npj computational materials

www.nature.com/npjcompumats

ARTICLE OPEN

Obtaining auxetic and isotropic metamaterials in counterintuitive design spaces: an automated optimization approach and experimental characterization

Timon Meier[1,3], Runxuan Li[1,3], Stefanos Mavrikos[1], Brian Blankenship[1], Zacharias Vangelatos[1], M. Erden Yildizdag[2] and Costas P. Grigoropoulos[1]✉

Recent advancements in manufacturing, finite element analysis (FEA), and optimization techniques have expanded the design possibilities for metamaterials, including isotropic and auxetic structures, known for applications like energy absorption due to their unique deformation mechanism and consistent behavior under varying loads. However, achieving simultaneous control of multiple properties, such as optimal isotropic and auxetic characteristics, remains challenging. This paper introduces a systematic design approach that combines modeling, FEA, genetic algorithm, and optimization to create tailored mechanical behavior in metamaterials. Through strategically arranging 8 distinct neither isotropic nor auxetic unit cell states, the stiffness tensor in a $5 \times 5 \times 5$ cubic symmetric lattice structure is controlled. Employing the NSGA-II genetic algorithm and automated modeling, we yield metamaterial lattice structures possessing both desired isotropic and auxetic properties. Multiphoton lithography fabrication and experimental characterization of the optimized metamaterial highlights a practical real-world use and confirms the close correlation between theoretical and experimental data.

npj Computational Materials (2024)10:3 ; https://doi.org/10.1038/s41524-023-01186-2

INTRODUCTION

The design of mechanical materials with tailored properties has been subject of significant interest in recent years, driven by advancements in three-dimensional manufacturing processes and optimization techniques. Three-dimensional manufacturing, such as multiphoton polymerization, has enabled the fabrication of complex geometries with sub-micron resolution at increasingly high volumetric print rates[1,2]. Incorporating holography technologies into multiphoton lithography (MPL) has further enhanced the creation of larger arrays of periodic structures while maintaining high feature resolution[3,4]. These advancements have enabled the manufacture of scalable architectures that surpass the bulk material properties of natural materials and might eventually lead to the widespread adoption of macroscale metamaterials in practical applications[5]. Modifying material feature sizes at the nanometer scale introduces a significant advantage to mechanical properties, known as the size effect. Certain nanomaterials exhibit extraordinary properties, such as increased strength compared to their bulk counterparts[6,7]. These exceptional characteristics make metamaterials highly suitable for a wide range of engineering applications, including ultralight materials[8,9], ultrastrong materials[10], reconfigurable materials[11], ultraelastic materials[12,13], high-energy absorption materials[14], fluidics[15], optics[16], and more.

Moreover, the creation of flexible structures possessing tailored mechanical properties has led to the development of bio-inspired designs, thereby enhancing the characteristics of inherently weaker bulk materials to a significant degree[17]. Many materials found in nature display fascinating properties that cannot be replicated by conventional materials. These natural materials, have evolved over millions of years, developing optimized architectures that span multiple hierarchies and length scales[18]. For example, bone exhibits a highly complex porous architecture that combines exceptional strength, toughness, low weight, and remarkable self-healing capabilities. These outstanding properties are mainly due to its composite nature, consisting of stiff and soft building blocks, and to its hierarchical organization, which consists of multiple structures across different length scales. Similar examples include the deep sea sponge *Euplectella aspergillum* featuring a spiral hierarchical design that exhibits remarkable resilience to buckling[19]. Another example is the snail *Chrysomallon squamiferum*, characterized by a multilayered structure that imparts toughness and in-plane isotropy, along with suture structures that regulate flexibility and strength[20]. The isotropic nature of these structures grants exceptional mechanical properties in all directions, making them suitable for applications with unknown or variable loading directions[21]. In addition, nature showcases auxetic behavior, where materials exhibit negative Poisson's ratios by expanding in transverse directions when subjected to axial loading. This unique characteristic is exemplified in the turtle shell, allowing it to efficiently absorb energy, withstand significant deformations without fracturing, and maintain uniform crushing load distribution[22]. This behavior can also be observed in salamanders, which can swell to prevent excessive tearing forces on their skin during quick movements to evade predators[23]. Snakes exhibit a similar phenomenon in their skin, utilizing non-Newtonian swelling for concertina movement, enabling progressive changes in cell turgor and body elongation[24,25].

Mimicking these structures holds the potential to significantly enhance material performance[26]. Among various structural designs, truss-like and lattice structures have garnered considerable attention due to their ability to mimic natural crystal structures and exhibit enhanced mechanical behavior[27–29]. Lattice structures, comprised of interconnected struts arranged in repeating patterns, offer advantages such as high strength-to-weight

[1]Laser Thermal Laboratory, Department of Mechanical Engineering, University of California, Berkeley 94720-1740 California, USA. [2]Faculty of Naval Architecture and Ocean Engineering, Istanbul Technical University, Istanbul 34469, Turkey. [3]These authors contributed equally: Timon Meier, Runxuan Li. ✉email: cgrigoro@berkeley.edu

ratio, energy absorption capabilities, and structural stability[30]. Designing and optimizing lattice structures have become essential in aerospace, automotive, biomedical, and energy systems. Special emphasis has been placed on the design of isotropic and auxetic lattice structures[31–33]. However, achieving systematic design of optimal lattice structures with multiple desired mechanical properties remains a challenging task. Conventional design methods relying on trial and error, or intuition[34–36] can be time-consuming, costly, and may not guarantee optimal performance. Therefore, there is a growing need for systematic design approaches capable of efficiently searching for optimal lattice structures that meet desired mechanical properties while satisfying specific design constraints.

In recent years, optimization methods have been employed to investigate and understand controlled elastic properties in various structures. Techniques such as topology optimization[37–41], artificial neural networks with genetic algorithms (GA)[42,43], and machine learning[44,45] have become essential tools in metamaterial design. Chen, W. et al. demonstrated the improvement of mechanical stiffness in materials through topology optimization, designing isotropic lattices based on continuum finite element analysis (FEA) and utilizing projection microstereolithography for fabrication and characterization[37]. Chen, D. et al. clustered 15,000 microstructures into families, from which parameterized templates were extracted for generating new complex microstructure designs, demonstrated through auxetic designs[38]. Agrawal et al. proposed a topology optimization method for designing metamaterials with negative Poisson's ratio, considering material property uncertainties in a linear elastic base material[39]. Tancogne-Dejean et al. designed elastically-isotropic structures by combining elementary cubic truss lattices, including Simple Cubic, Body-Centered Cubic, and Face-Centered Cubic structures[40]. Panetta et al. presented a combinatorial search over topologies followed by shape optimization, exploring a space of truss-like, symmetric 3D patterns. These patterns enable the fabrication of objects with specific mechanical behaviors and can be extended to create anisotropic patterns with target orthotropic properties[41]. Contrasting traditional topology optimization approaches, Chang et al. employed neural networks and a GA for designing auxetic metamaterials with specific Poisson's ratio. Their model, trained on a dataset from finite element simulations, established mapping relationships to optimize microstructure parameters for desired Poisson's ratios, demonstrating effectiveness through comparisons with tensile experiments and FEA[42]. Chen et al. applied multi-objective optimization using Non-dominated Sorting Genetic Algorithm (NSGA-II) assisted by an elliptical basis function neural network, coupled with FEA, to design a new class of isotropic and reusable cork-like metamaterial with an isotropic Poisson's ratio close to zero[43]. Zheng et al. introduced an inverse design method for auxetic metamaterials using deep learning, employing a conditional generative adversarial network to generate auxetic metamaterials with user-defined Poisson's ratio, validated through finite element method simulations and uniaxial compression tests[44]. Wilt et al. utilized machine learning to enhance the design of compliant auxetic 2D metamaterials with negative Poisson's ratio, with confirmation of mechanical behavior through FEA and experimental validation[45]. Despite these advancements, it is crucial to address certain challenges and limitations in the field. Firstly, some designed structures lack experimental validation[39], while others require substantial data to explore the design space, resulting in high computational costs or design limitations for 2D or homogeneous 3D structures[38,42,44,45]. Additionally, all studies incorporate feature dimensions as a design variable which is theoretically advantageous but poses practical challenges in fabrication and limits experimental validation. The presence of overlapping elements and variable dimensions introduces complexity, leading to significant discrepancies between designed and fabricated structures. For instance, Chen, D. et al. observed a substantial thickening of up to 50% compared to their smallest feature sizes, causing substantial stiffening and deviation from the modeled Poisson's ratio[38]. Consequently, achieving higher precision in manufacturing processes or adopting larger overall dimensions becomes imperative. Moreover, simulating intricate designs is computationally expensive, significantly elevating the overall costs associated with achieving optimal designs. Furthermore, certain designs only optimize for one property[37,40,41]. The implementation of topology optimization, particularly within FEA, is complex, relying on intricate mathematical models, and in the referenced studies, is confined to single-objective optimization.

In our previous work[46], we presented a Bayesian Optimization scheme for designing non-monolithic architected materials with controlled behavior, using discrete and qualitative design variables. By utilizing 69 data points, we successfully obtained the optimum structure possessing Cauchy symmetry from a discrete design space containing 5^{10} structures. These structures were then fabricated and experimentally validated. However, the study still had certain limitations that will be addressed in this paper. Firstly, the design problem focused solely on single-objective optimization, disregarding the potential for multi-objective optimization. Additionally, the FEA simulations were performed manually in each iteration loop, which restricted the number of input variables and the overall size of the discrete design space. These limitations were necessary to ensure that the optimization problem remained computationally feasible and manually manageable. The objective of this study is to expand the scope by addressing a fully automated multi-objective design optimization problem that encompasses a larger design space. In this paper, we propose an approach for the systematic design of lattice structures with tailored elastic behavior using a GA optimization framework. By automating the entire process, our approach becomes applicable to a wider range of optimization cases that require increased computational resources and iterations. Specifically, we focus on tailoring the behavior of architected metamaterials by targeting the design objectives of isotropy and auxeticity, with a particular emphasis on achieving a zero Poisson's ratio. We construct a cubic symmetric microlattice structure with dimensions of $5 \times 5 \times 5$ and a size of $50 \times 50 \times 50$ μm. The lattice structures consist of eight different unit cell states, each featuring a constant beam diameter to facilitate fabrication, ensuring microscale precision and repeatable performance at the highest levels of accuracy. Moreover, none of the monolithic cells are isotropic or auxetic individually to avoid potential biases or intuitive outcomes that might occur during the optimization. This design choice results in a large counterintuitive combinatorial design space, providing flexibility in achieving desired mechanical properties. To solve this complex multi-objective problem, we utilize the well-known and openly available NSGA-II[47] from the pymoo library[48]. NSGA-II efficiently handles the expensive and multi-objective nature of the problem, operating within the combinatorial design space while considering predefined design constraints. Furthermore NSGA-II is versatile and can be applied to various types of optimization problems without requiring specific problem knowledge. This makes it a widely applicable algorithm that can easily be adapted for other frameworks or to reproduce these results. Automated FEA simulations are performed to investigate the mechanical response and calculate the elastic properties of the lattice. These results are then used to evaluate the objective cost functions and serve as input for the optimization algorithm. To validate the effectiveness of our approach and highlight a real world application, we fabricate micro-scale structures using MPL. In-situ scanning electron microscopy (SEM) micro-indentation testing is conducted to assess the mechanical response and verify the validity of our finite element model. The comprehensive results demonstrate how discrete unit cell states can be leveraged to optimize the behavior of complex 3D structures, leading to the creation of metamaterials with extraordinary targeted mechanical properties. In essence, our work achieves the creation of an isotropic and auxetic metamaterial within a discrete and counterintuitive design space. This is accomplished by rearranging basic unit cell states in an array while maintaining constant feature sizes and dimensions, which

facilitate its fabrication at the highest accuracy. Our comprehensive methodology integrates automated design, FEA, and optimization with MPL fabrication, and experimental characterization to validate the optimal structure. Notably, our approach is versatile and can be adopted by fellow researchers exploring diverse cost functions.

RESULTS

Framework for systematic lattice design

Metamaterials with cubic symmetry have attracted considerable attention due to the prevalence of extensively studied structures such as the Diamond, Octet Truss, and Kelvin foam[49]. Thereby, the stress tensor $\boldsymbol{\sigma}$ is related to the strain tensor $\boldsymbol{\varepsilon}$ in three-dimensional composites through the constitutive law of linear elasticity. This relationship is expressed using an effective order-4 symmetric stiffness tensor $\mathbf{C}$ where

$$\boldsymbol{\sigma} = \mathbf{C}\boldsymbol{\varepsilon}. \tag{1}$$

When considering cubic symmetry, the effective stiffness tensor is characterized by only three independent elements: C_{11}, C_{12}, and C_{44}. C_{11} and C_{12} represent stiffness components related to normal stress, while C_{44} specifies the shear modulus for cubic symmetric structures. The effective stiffness tensor can be represented as[50]:

$$\mathbf{C} = \begin{bmatrix} C_{11} & C_{12} & C_{12} & 0 & 0 & 0 \\ & C_{11} & C_{12} & 0 & 0 & 0 \\ & & C_{11} & 0 & 0 & 0 \\ & & & C_{44} & 0 & 0 \\ & sym & & & C_{44} & 0 \\ & & & & & C_{44} \end{bmatrix} \tag{2}$$

The objective of this work is to develop an inverse design strategy for a non-monolithic microlattice composed of different discrete unit cell states with tailored elastic behavior. By utilizing fully automated FEA simulations and an open-source genetic optimization algorithm, various cost functions and objectives can be defined to achieve tailored behavior, such as high directional stiffness or Cauchy symmetry. These cost functions are determined based on the ratio or correlation between the stiffness tensor components C_{11}, C_{12} and C_{44}. This work concentrates on tackling the multi-objective design challenge of dually achieving isotropy and auxeticity, with a specific emphasis on attaining a Poisson's ratio of zero.

Isotropic materials exhibit the same mechanical properties in all directions, making them highly desirable for achieving uniform load distribution and structural stability. To quantify the variance for the stiffness in different directions of cubic structures, the Zener ratio A is used and defined as[51,52]:

$$A = \frac{2C_{44}}{C_{11}-C_{12}} \tag{3}$$

Structures with a Zener ratio value of $A = 1$ are considered isotropic. Accordingly, the first cost function to minimize for the optimization problem is defined as:

$$f_1(\boldsymbol{\omega}) = |C_{11} - C_{12} - 2C_{44}| \tag{4}$$

The Poisson's ratio for compression along the principal axes can be expressed as[43]:

$$v = \frac{C_{12}}{C_{11}+C_{12}} \tag{5}$$

Therefore, to achieve an auxetic structure with a zero Poisson's ratio, the second cost function to minimize for the multi-objective optimization problem is defined as:

$$f_2(\boldsymbol{\omega}) = \left|\frac{C_{12}}{C_{11}+C_{12}}\right| \tag{6}$$

The design strategy of identifying an optimal isotropic and auxetic, zero Poisson's ratio structure is depicted in Fig. 1. During the course of this procedure, we utilize 8 distinct anisotropic and non-auxetic unit cells, depicted in different colors in Fig. 1a, denoted as A, B, C, D, E, F, G and H. To simplify the process, we choose unit cell states that possess cubic symmetry itself, facilitating their systematic assembly into a bulk microlattice. Furthermore, all unit cells are face-centered and incorporate nodes at the center of each of the six faces. This arrangement allows for a flexible and arbitrary combination of unit cells within the lattice, ensuring that all unit cells are connected, at the very least at this center face node. To achieve compatibility with the feature resolution of the MPL apparatus, the unit cells are designed to be $10 \times 10 \times 10$ μm in size. These unit cells are arranged in a $5 \times 5 \times 5$ array. The selection of unit cells was deliberate, incorporating well-studied designs like the octet truss[53], alongside other studied face-centered and body-centered configurations[54,55]. Furthermore, our choice of 8 distinct unit cell states ensures a diverse range of stiffness behaviors, establishing a versatile design space, as it will be described in the discussion section and shown in Fig. 9. Although expanding the design space is feasible by opting for a larger array size, such as $7 \times 7 \times 7$ or incorporating more input unit cell states, this extension poses challenges due to heightened computational demands in both optimization and FEA, along with the imperative for more sophisticated experimental validation due to the increase of the geometry. To ensure the boundary condition of cubic symmetry, ten positions within the $5 \times 5 \times 5$ array can be assigned independently as shown in Fig. 1b. All other positions are determined based on the symmetry requirement of the structure. This means that the same type of unit cell, for example, is positioned in all corners of the structure. As a result, specific microlattice configurations can be uniquely described by a 10-component $\boldsymbol{\omega}$-vector $[\omega_1, ..., \omega_{10}]$, where each component can take values from A to H according to the chosen unit cell. Thus the structure shown in Fig. 1b can uniquely be described by $\boldsymbol{\omega}$ = [H G B E D G D B D A]. The selection of this layout scheme offers two significant advantages. Firstly, it reduces the stress tensor to three independent stiffness values, thereby simplifying the number of simulations and tests needed to obtain these stiffness values and assess whether isotropy and auxeticity has been achieved. This reduction in complexity streamlines the analysis process. Secondly, the chosen layout scheme significantly decreases the number of possible combinations of lattices. By imposing the restriction of cubic symmetry for the $5 \times 5 \times 5$ lattice with 8 distinct unit cells, the design space is reduced from a staggering 8^{125} states to $8^{10} \approx 1.073$ billion states when all symmetry planes of the structure are taken into consideration. This reduction in the design space allows for a more focused exploration of potential lattice configurations and facilitates more efficient optimization strategies. Figure 1c shows the multi-objective optimization process that progresses from random structures towards attaining the optimum of an isotropic and auxetic lattice structure. The schematic showcases this transition using a stiffness map, where the initial arbitrary shape evolves into a sphere (indicating perfect isotropy), and the colors gradually shifts from high Poisson's ratio (red) to auxeticity (blue).

Figure 2 shows the schematic framework of the design and optimization setup. During the design process (Fig. 2a), specific parameters like the lattice size and dimensions are established initially and maintain constant throughout. Subsequently, a wide range of unique unit cell states can be defined, each of which is mathematically represented by lines. Following this, arbitrary and multiple-cost functions can be formulated for optimization purposes. In our case, we illustrate this using 8-unit cell states, a

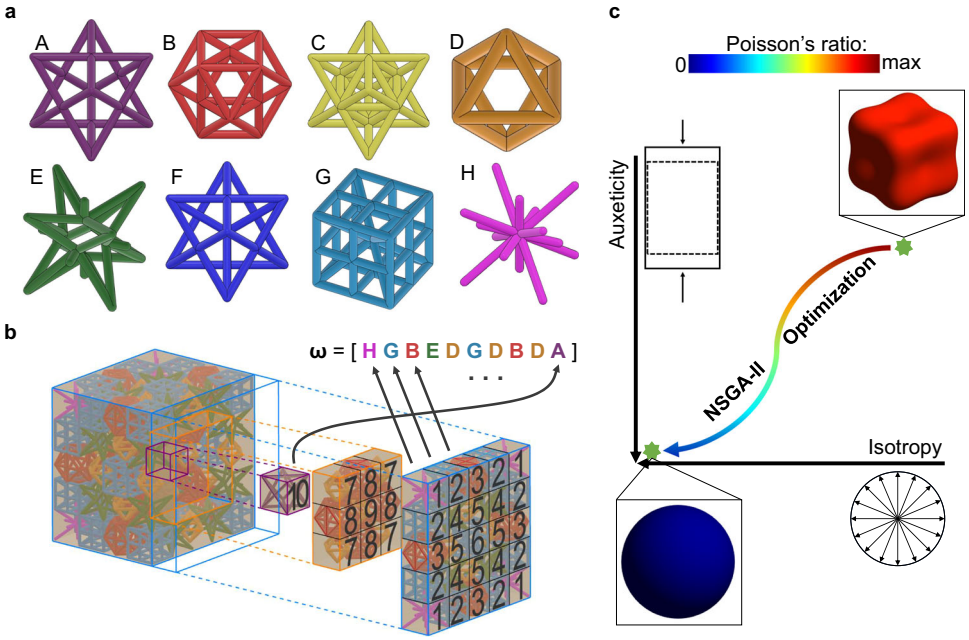

Fig. 1 Design space of the optimization setup. a Input Classification: 8 types of cubic symmetric input cells, labeled A - H and color coded. Cells are face centered and contain nodes in the center of each face. This arrangement ensures compatible connectivity between multiple cells within a lattice, while preventing any overlapping of beam elements. **b** Cells are used to construct $5 \times 5 \times 5$ cubic symmetric lattice. The symmetry constraint leads to 10 arbitrary positions (labeled 1 - 10) where different unit cell states can be placed. Thus, unique lattice configurations can be described by 10-component $\boldsymbol{\omega}$-vector. **c** Diagram illustrates the multi-objective optimization problem of achieving an isotropic and auxetic lattice structure. The schematic showcases this transition using a stiffness map, where the initial arbitrary shape (top right) evolves into a sphere (bottom left), indicating perfect isotropy, and the colors gradually shifts from high Poisson's ratio (red) to auxeticity (blue).

cubic symmetric array of $5 \times 5 \times 5$, and the multi-objective design problem opting for isotropy and auxeticity. In the optimization process (Fig. 2b), the NSGA-II GA[47] is employed to explore the design space and discover a micro lattice design that is both isotropic and auxetic. Using the population data generated by the optimization algorithm, unit cells are arranged in a specific configuration to create unique cubic symmetric lattices. Fabricating and mechanically testing every structure would be infeasible given the time it takes to fabricate and test them. Additionally, mechanical testing introduces noise into the results that can impact the required data quantity. Therefore, we opt to employ FEA to calculate stiffness components. To approach an optimal solution, we input the calculated stiffness values from the FEA simulations to evaluate the cost functions. The convergence process of lattice evolution, FEA simulation, and optimization is implemented within a Python environment that utilizes executables from ANSYS® and pymoo[48]. We define an optimal solution as one that deviates by less than 1% from the desired levels of isotropy and auxeticity. This tolerance threshold serves as the criterion for determining the quality of the solution. The entire optimization process is automated and does not necessitate any user input.

Once the algorithm converged on an acceptable solution, the optimum is fabricated and subject to mechanical testing. A hybrid organic-inorganic resin was utilized in the fabrication process. Previous studies[56] have shown that stiffness measurements obtained through mechanical testing are limited to the elastic range, as the photoresist material is highly susceptible to variations in fabrication parameters, making it sensitive in the plastic domain. Inside a SEM, mechanical testing and structural analysis are performed. Detailed information about the FEA model, applied boundary conditions to calculate the stiffness components, optimization, material properties, fabrication and testing procedures can be found in the Methods section and Supplementary Figure 1 and Figure 2.

Convergence of the algorithm

The results and convergence of utilizing the NSGA-II algorithm to optimize the micro lattice for the multi-objective of isotropic and auxetic behavior are depicted in Fig. 3. The problem is initialized with 8 structures, each composed of a single unit cell state. The sequential history of the normalized multi-objective optimization cost is illustrated, which is calculated as the ratio of the current optimum to the best input unit cell array. The input cell array optimum, in our case unit cell state H, is the equally weighted value of the two objective functions for isotropy and auxeticity

$$\text{Euclidean Cost} = \sqrt{f_1(\boldsymbol{\omega})^2 + f_2(\boldsymbol{\omega})^2}. \tag{7}$$

It is noted that all input unit cells exhibit anisotropic behavior and possess a positive Poisson's ratio ranging from 0.14 to 0.39. Using the provided input data from the sampling of the search space, we can determine that the average cost function value is represented by the mean $\bar{x} = 2.664$. Additionally, the variance of the search space is denoted as $s^2 = 1.264$. The cost function value of an optimal isotropic and auxetic structure is defined as zero. By achieving full automation of the optimization and FEA simulation process, rapid iteration loop are made possible, with each iteration requiring approximately five minutes. This capability enables the exploration of the design space with several thousand iterations within a relatively short time frame.

The insets in Fig. 3 illustrate the evolution of the stiffness map and Poisson's ratio of the structures over the iterations, ultimately yielding to an isotropic (perfect spherical shape) and auxetic (blue color) optimum after 2399 iteration loops. The sequence $\boldsymbol{\omega}_{opt}$ = [H G B E D G D B D A] represents the mathematical representation of the optimum structure, as depicted in Fig. 1b and shown in the next section. It is worth noting that the optimized structure does not exhibit a distinct pattern or layer arrangement that demonstrates periodicity or

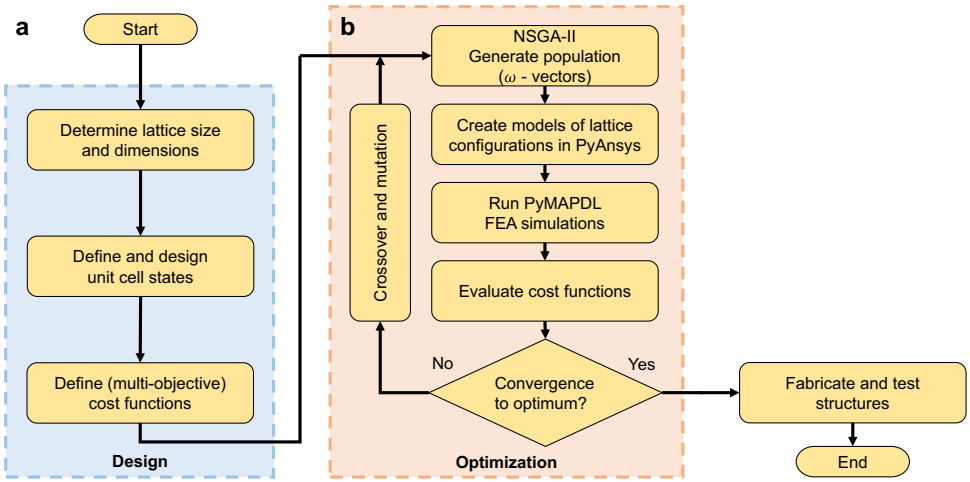

Fig. 2 Flowchart and pseudo code of work. a Design and Problem Setup: The initial step involves setting the parameters, such as lattice dimensions, and designing and defining the input unit cell states. This one-time setup allows for flexibility in defining various cost functions and optimization goals, making the setup adaptable to a wide range of applications. **b** Optimization: The Python environment enables a fully automated process for FEA simulation and optimization. The NSGA-II algorithm and Python simulation code generates a population, performs FEA simulation, evaluates cost functions, and continues iterating until convergence is attained. To ensure the accuracy of the theoretical results, the optimal structure is fabricated and subjected to testing for validation purposes.

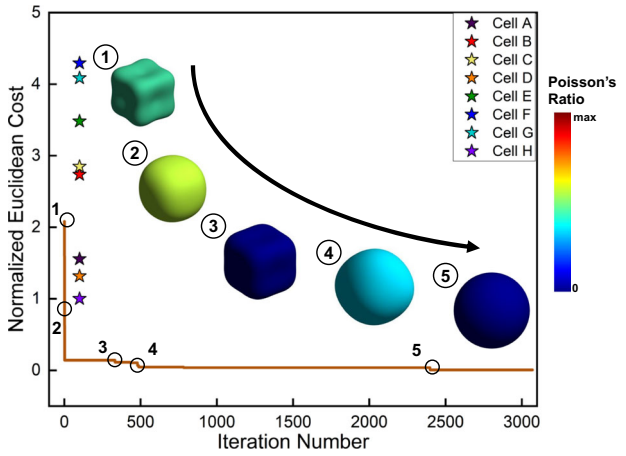

Fig. 3 Convergence of the multiobjective optimization process. The vertical axis represents the normalized Euclidean cost for isotropy and auxeticity, calculated as the ratio of the current optimum to the best input unit cell lattice (Cell H), with the design objective defined as a cost of 0. The horizontal axis corresponds to the number of function iterations. Insets illustrate the evolution of structures using stiffness maps towards the optimal isotropic (perfect sphere shape) and auxetic (blue color) configurations as the iteration number increases.

uniformity in any particular direction, making its design counter-intuitive. In order to experimentally validate the optimized structure, all input unit cell structures, and the optimized structure, were fabricated using the MPL apparatus described in the Methods section. To ensure uniformity in the cross-section of the structures, a single batch of resin was utilized, and the fabrication process was completed within a 24-hour period. The laser power, writing speeds, and beam alignment were carefully controlled and kept constant throughout the fabrication process. Moreover, to ensure repeatability, each beam member was fabricated by performing multiple passes of the laser beam at precisely the same location. This approach guarantees the uniformity and reliability of the fabricated structures for subsequent testing and analysis.

Properties of the optimum and their corresponding input cells

Figure 4 displays images obtained from the Helium Ion Microscope (HIM) which provides high-resolution imaging and a large depth of focus. It includes a top view of all monolithic structures fabricated with the MPL setup in a row and a detailed isometric view of each structure A - H. Figure 5 shows the fabricated optimum structure from an isometric (a) and top view (b). In the top view the different unit cell states A - H are color-coded according to Fig. 1a and the internal nonuniformity can be clearly observed.

In order to determine the elastic constants from the experimental findings, the directional elastic properties were derived using a methodology outlined elsewhere[57]. The directional Young's Modulus, Poisson's ratio, and Shear Modulus can be calculated using the following equations:

$$E = \frac{1}{S_{11}} \qquad v = -\frac{S_{12}}{S_{11}} \qquad G = \frac{1}{S_{44}} \tag{8}$$

where S_{11}, S_{12}, S_{44} is the compliance tensor to the stiffness matrix $\mathbf{C}$ and S_{12} indicates the direction normal to the loading. In order to validate FEA results and obtain measurements for the Young's modulus and Poisson's ratio, compression tests were performed for all monolithic structures and the optimum. Figure 6a showcases the characteristic stress-strain curves obtained from the compression tests conducted on all input cell arrays and the optimum structure.

By analyzing the experimental curves, the Young's modulus can be determined. Figure 6b presents a representative frame captured during the compression measurement. Furthermore, by referring to the Supplementary Videos 1–9, the Poisson's ratios of the structures can be determined graphically by examining the relationship between lateral and transversal strain. The values for Young's modulus and Poisson's ratio of the optimum structure for the elastic regime and small deformations were found to be $E = 193 \pm 9$ MPa and $v \approx 0$, which closely aligns with the theoretical estimate from the FEA simulations of $E = 181$ MPa and $v = 0.01$.

DISCUSSION

We introduced a systematic design approach aimed at creating optimal isotropic and auxetic lattice structures through multi-objective optimization. To explore a vast design space consisting

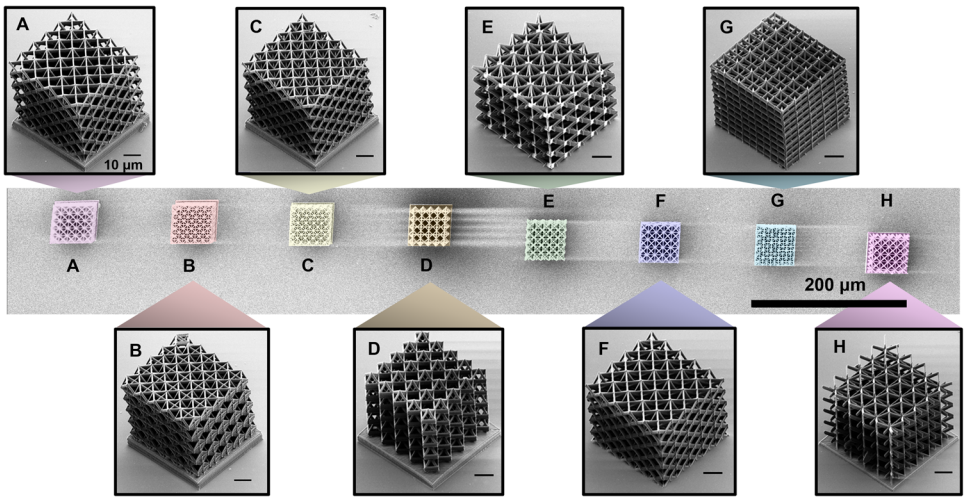

Fig. 4 HIM images of input cell arrays A - H. The top view displays the states of all cells in a row, with structures color-coded as indicated in Fig. 1a. Detailed isometric views are shown above and below the corresponding cells in the top view.

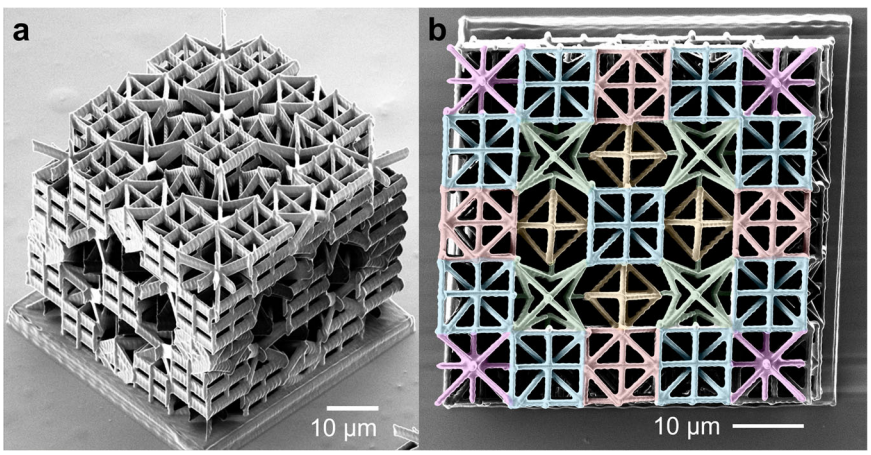

Fig. 5 HIM image of optimal isotropic and auxetic structure. a Orthogonal view of optimum. **b** Top view of optimum showing color-coded different unit cell states, emphasizing the non-intuitive result of the optimization.

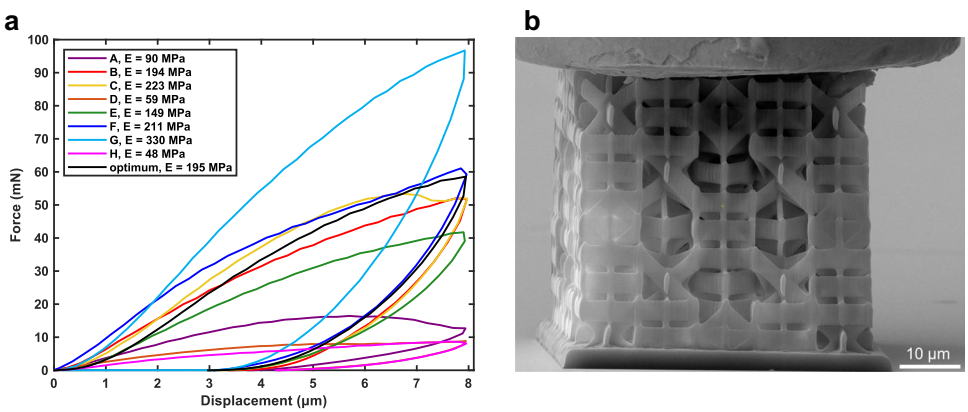

Fig. 6 Mechanical testing of structures. a Compression tests of structures A - H and the optimum configuration, measured using a PI-87 Picoindenter. The mechanical loading responses are depicted, and the slopes of the curves are utilized for validating the cost functions and optimization process. **b** Representative frame of the compression measurement for the optimum configuration, illustrating the application of a compressive load by the indenter in lateral direction.

of billions of possible combinations, we employed a GA and worked within a discrete, qualitative counterintuitive design space. The successful implementation of this approach allowed us to effectively control the stiffness tensor in the lattice structure, achieving both isotropy and auxeticity. By formulating the problem as an optimization task and defining appropriate cost functions, we utilized the GA to inversely evolve lattice structures towards their optimal configurations. Although the number of

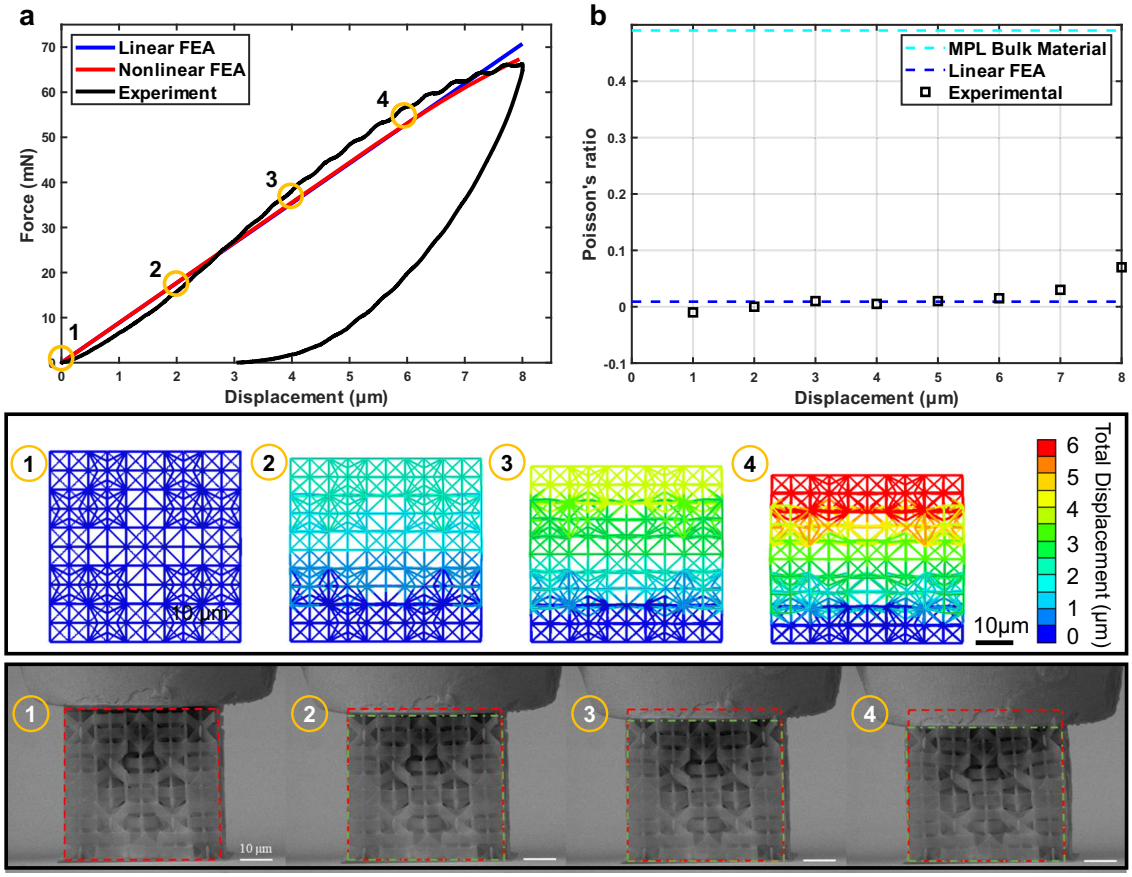

Fig. 7 Experimental compression test data of the optimal structure is presented, along with video captures and a comparison to theoretical FEA results. a Illustrates a representative force-displacement curve for the compression tests of the optimum structure, combining both linear FEA used for optimization and an additional nonlinear FEA analysis. The insets show various deformation states throughout the force-displacement curves for the nonlinear FEA analysis and experimental compression tests. **b** Compares the Poisson's ratio with the compressive displacement for MPL bulk material, FEA and measured experimental data. The experimental data demonstrates agreement with the simulation results, indicating a Poisson's ratio close to the optimization goal of zero.

iteration loops required to find the optimum was relatively high compared to previous studies, the use of automated simulation and optimization processes, leveraging PyAnsys and other open-source libraries in a Python environment, significantly reduced the overall iteration time. Each iteration took only a few minutes, resulting in a relatively short overall optimization time that could be further reduced through parallel computing. The problem setup and flexibility of the framework also allows for easy adjustment of cost functions to achieve different tailored mechanical behaviors, making the optimization scheme efficient, reliable, and versatile. Our results provide evidence for the effectiveness of the GA in generating lattice structures with enhanced mechanical properties. The absence of any identifiable pattern in the optimal structure, which possesses both isotropy and auxetic behavior, highlights the importance of optimization in designing non-monolithic structures. This further emphasizes the versatility of the GA approach in addressing complex and challenging multi-objective problems that lack intuitive or mechanical principles.

To gain insights into the mechanical behavior of the ideal structure, we examined the force-displacement curve in conjunction with the video captures, which effectively highlights the impact of auxeticity. Figure 7 displays the results of the experimental compression test conducted on the optimal structure, along with video captures and a comparison to theoretical FEA outcomes. Figure 7a illustrates a representative force-displacement curve obtained from the compression tests, showcasing the linear FEA utilized for optimization, as well as an additional nonlinear FEA analysis. Notably, all curves exhibit a close correlation. The insets at the bottom of the figure highlight various deformation states observed during the nonlinear FEA analysis and experimental compression tests. A nearly zero Poisson's ratio is observed for both cases at small deformations. This agreement is further depicted in Fig. 7b, which compares the Poisson's ratios for the FEA and measured experimental data. Despite originating from a MPL bulk material with a high Poisson's ratio of 0.499, the targeted structural design achieves an almost 0 Poisson's ratio and the experimental data aligns well with simulation results. The mechanical compression response of the optimized structure is illustrated through the correlation between the reaction force and the maximum principal stress in Fig. 8. Further insights are provided through stress distribution and deformation patterns on the right side of the plot, showcasing significant variations across the structure. It is observed that the stress distribution within the lattice structure is not uniform across entire rows but rather localized in specific sections. This pattern arises due to the nontrivial configuration of various unit cell states within the lattice structure. Examination of the region experiencing the highest principal stress reveals potential weak points prone to buckling and failure of beam elements. Exploiting this unconventional behavior can be used for the precise control of failure mechanisms on a localized level.

Additionally, Fig. 9 illustrates the directional stiffness maps and Poisson's ratios in spherical coordinates for both the initial

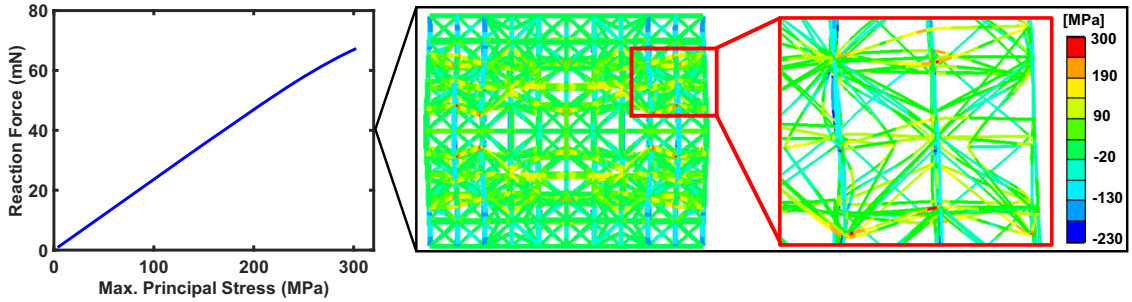

Fig. 8 Plot illustrating the mechanical compression response of the optimum structure, depicting the relationship between reaction force and maximum principal stress. The stress distribution and deformation under load are shown on the right side, highlighting variations across the structure, with a detailed view of the region experiencing the highest principal stress. The presence of excessive principal stress leads to buckling and eventual failure of beam elements. This unconventional behavior can be used for the precise control of failure mechanisms on a localized level.

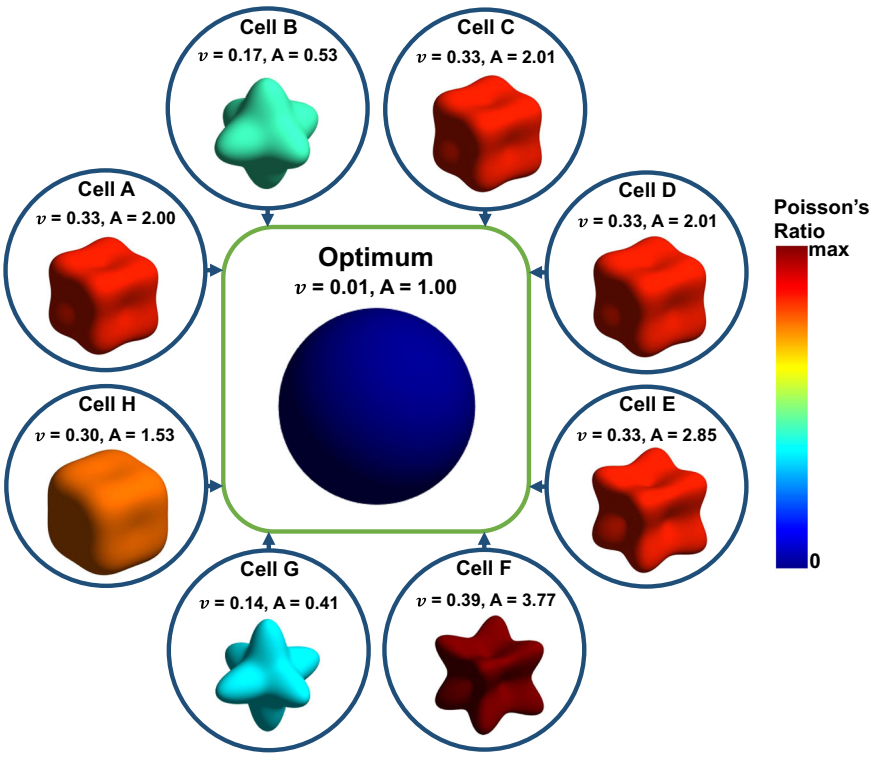

Fig. 9 Directional stiffness map, illustrating the properties of monolithic structures and the optimal structure obtained through the optimization process. It is observed that all monolithic structures possess a positive Poisson's ratio ($\nu \geq 0.14$) and none of them approaches isotropy individually. However, when combined, they yield an optimal structure that achieves both isotropy and auxetic behavior, characterized by a Poisson's ratio of $\nu = 0.01$ and a Zener ratio of $A = 1$.

monolithic structures and the optimum structure. The anisotropy of the structures is assessed using the Zener ratio, while the value of ν indicates the Poisson's ratios. The plots clearly demonstrate how a design space limited to anisotropic structures ($A \ncong 1$) and positive Poisson's ratio ($\nu \geq 0.14$) in the monolithic input cells, through merging in a unifying lattice structure to can lead to an optimal result that is both, isotropic ($A = 1$) and auxetic ($\nu = 0.01$). These findings further emphasize the role of optimization in uncovering optimal points that cannot be determined through intuition. The elastic behavior of the optimum structure remains reversible until reaching a strain of approximately 7% where slight weakening is observed, primarily attributable to imperfections in the fabrication process. When comparing the experimental and FEA force displacement data for all monolithic structures and the optimum structure, an average error of 8% is observed for Young's modulus and Poisson's ratio. This close correlation between the theoretical and experimental data in the compression tests of multiple structures, provides a reasonable level of confidence in the validity of the FEA results for shear stress and, consequently, the whole optimization results.

This study introduces a systematic design approach that offers engineers and researchers a valuable tool for creating lattice structures with customized and tailored mechanical properties. By utilizing the GA, we achieved efficient exploration of the design space, leading to optimal solutions and substantial time and resource savings compared to traditional trial-and-error methods. It is important to note that the optimization process heavily relies on the selection of appropriate design variables, objective functions, and constraints. These parameters significantly impact the outcome and resulting lattice structures, emphasizing the need for a thorough understanding of the underlying mechanics and design requirements to obtain meaningful results. While this

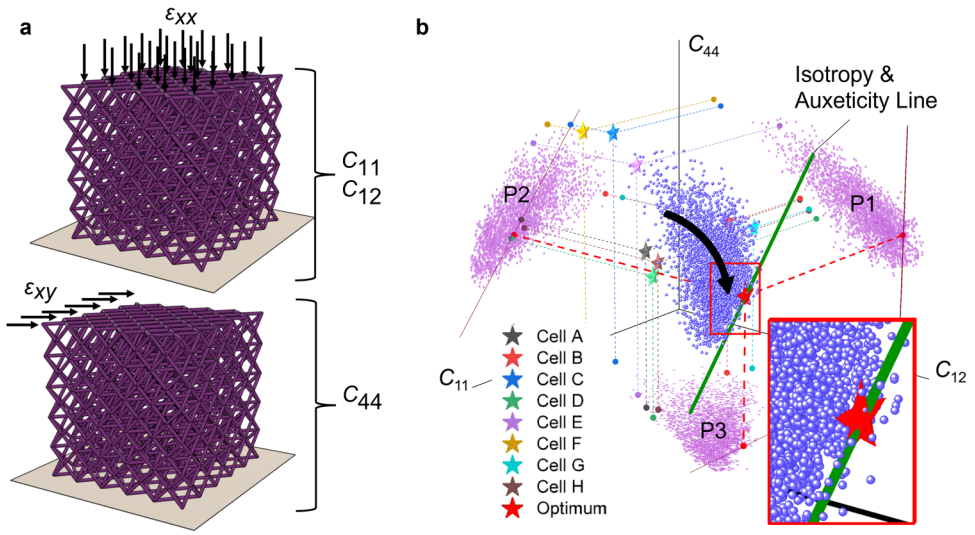

Fig. 10 FEA load cases and optimization results. a Compression and shear FEA load case to determine all three independent stiffness tensor elements C_{11}, C_{12}, C_{44} of cubic symmetric lattices. **b** The stiffness values for all input unit cells and optimization iterations are visualized in three-dimensional space. The green line represents the multi-objective optimization goal of isotropy and auxeticity. The iterations (depicted as blue spheres) progressively converge towards the optimal structure, which lies on the line as shown in the inset. P1, P2, and P3 represent 2D projections of the data points onto the C_{11}, C_{12}, C_{44} planes, facilitating the examination of individual behaviors throughout the optimization process.

research primarily focused on isotropic and auxetic properties, the methodology presented can be extended to explore other mechanical characteristics, such as stiffness, strength, or damping, depending on specific application requirements. The versatility of the GA enables the optimization of lattice structures for a wide range of mechanical properties. Furthermore, the framework we have introduced holds the potential to seamlessly integrate with methodologies like the one presented by Makatura et al.[58]. This approach enables the rapid design of intricate cellular metamaterials within a user-friendly environment. By incorporating an inverse design methodology, our frameworks empowers users to specify their desired material properties and employ an algorithm to discover the most optimal metamaterial structure accordingly. To advance and broaden the scope of our research, several areas warrant further exploration. Firstly, exploring alternative optimization techniques and evolutionary algorithms could enhance the optimization process. Secondly, expanding the design space by incorporating more complex unit cell designs, additional design parameters, and larger arrays, while considering constraints for manufacturability and material-specific considerations, would ensure practical feasibility. Thirdly, extending the methodology to account for dynamic loading conditions, including plastic deformation properties, reversibility, energy absorption, and buckling, enables the design of lattice structures optimized for dynamic performance[2,59]. Additionally, conducting experimental validation of the optimized lattice structures and exploring application-specific optimization would provide real-world validation and tailored solutions. From a fabrication standpoint, exploring advanced additive manufacturing techniques such as projection lithography[60] could increase the printing area and enable the efficient fabrication of high-resolution mesoscale structures. Lastly, investigating multi-objective optimization approaches that balance complex criteria involving mechanical, thermal, and optical properties would further enhance the systematic design approach. Pursuing these future research directions would enable the creation of lattice structures with optimized properties for various applications, particularly in optics, MEMS, flexible electronics, and for meeting requirements for ultralight or ultrastiff structures[61,62].

METHODS

Finite element analysis and optimization

Figure 10 shows the correlation between simulations, calculation of the cost function and the optimization process. In order to analyze the mechanical properties of the lattice structure, we employed FEA simulations. The model and its mesh were created parametrically in ANSYS® Mechanical™ version 2021 R1 using the ANSYS® Parametric Design Language (APDL). To enhance our analysis capabilities, we utilized PyMAPDL, a Python Application Programming Interface (API) under the PyAnsys umbrella, which granted us access to the local MAPDL solver and the simulation data it generated. Originally a standalone package, PyAnsys has transformed into a comprehensive collection of Python packages that enable seamless integration with ANSYS®. Hence, different lattice configurations can be easily conceived by changing geometric parameters in the code. This expanded functionality offers a wide range of possibilities, empowering us to construct models and initiate simulations alongside generative AI models and advanced statistical analysis. All of the structures called by the optimization algorithm were fully automatically designed and analyzed using the PyAnsys environment. For the FEA simulations, the beam lattices were assigned the following properties: an elastic modulus of 1.281 GPa and a Poisson's ratio of 0.4999. These parameters were utilized to accurately represent the mechanical behavior of the lattice structure in the analysis. The structures were meshed using 3D 2-Node elements of type BEAM188 with circular cross-sections. The element type is based on Timoshenko beam theory and includes shear-deformation effects. The average element size was selected by conducting a mesh convergence study and set to an element length of 0.5 μm. While the beam diameter remains constant throughout different unit cells to facilitate fabrication, the volume fraction varies among different arrays. However, as shown in Table 1, the relative density generally is below 20%, ensuring accurate modeling through 2-node beam elements. While structures with higher relative density tend to be more isotropic since the structure converges to the bulk material, it must be noted that our optimum that is both auxetic and isotropic has relative density similar to unit cells B, C, E, F and G. However, all of these monolithic unit cells are far from auxetic or isotropic, showcasing how the arrangement of unit cells in the 3D

Table 1. Volume fraction for different monolithic arrays A–H and the optimum structure.

Array	A	B	C	D	E	F	G	H	Optimum
Volume fraction	0.107	0.183	0.196	0.080	0.205	0.180	0.194	0.105	0.205

space is the dominant factor in the design of a both auxetic and isotropic structure.

By utilizing the same hardware system, the computation time using beam elements can be reduced by over 90% compared to 3D tetrahedral elements. Additionally, a study involving multiple lattice configurations demonstrates that the elastic constants are within a 5% range for the different mesh element types. For the calculation of all elastic components of a cubic symmetric structure, two load cases are needed. A compression load case to calculate the stiffness components C_{11}, C_{12} which relate to normal stresses and a shear load case for the calculation of C_{44} which specifies the shear modulus for a structure as shown in Fig. 10a. This methodology has been previously employed for the precise calculation of the polar stiffness map of structure, leading to a close correlation between theoretical and experimental results[52]. Two types of boundary conditions for compression, Eq. (9), and shear testing, Eq. (10), are defined. Take a normal strain ε_{xx} for instance, the boundary conditions were defined by[52]:

$$\Delta l_x|_{x=l_x} = 0.01 l_x, \qquad \Delta l_x|_{x=0} = \Delta l_y|_{y=l_y} = \Delta l_y|_{y=0} = \Delta l_z|_{z=l_z} = \Delta l_z|_{z=0} = 0 \tag{9}$$

which means the displacement in x axis is $0.01 l_x$ when $x = l_x$, and the displacements in all other directions are zeros. In the case of shear strain ε_{xy}, the boundary conditions were:

$$\begin{aligned} &\Delta l_x|_{z=l_x} = 0.005 l_z, \qquad \Delta l_z|_{x=l_z} = 0.005 l_x, \\ &\Delta l_z|_{x=0} = \Delta l_y|_{y=l_y} = \Delta l_y|_{y=0} = \Delta l_z|_{z=l_z} = \Delta l_x|_{z=0} = 0 \end{aligned} \tag{10}$$

The elastic stiffness components can be calculated by dividing the average strain ($\bar{\varepsilon}_{ij}$) through the average stress ($\bar{\sigma}_{ij}$)[63–65]:

$$C_{11} = \frac{\bar{\sigma}_{xx}}{\bar{\varepsilon}_{xx}} \qquad C_{12} = \frac{\bar{\sigma}_{yy}}{\bar{\varepsilon}_{xx}} \qquad C_{44} = \frac{\bar{\sigma}_{xy}}{\bar{\varepsilon}_{xy}} \tag{11}$$

The average stress and strain values are obtained by integrating over the volume or particularly all finite elements:

$$\bar{\varepsilon}_{ij} = \frac{1}{V}\int_V \varepsilon_{ij}\, dV \qquad \bar{\sigma}_{ij} = \frac{1}{V}\int_V \sigma_{ij}\, dV \tag{12}$$

To conduct uniaxial compression testing, an infinitely stiff plane is affixed to the top surface of the structure and displaced downward in the negative x direction. C_{11} is calculated by averaging σ_{xx} and C_{12} by averaging σ_{yy}. For shear testing, a lateral displacement is applied to an edge of the structure, and C_{44} is calculated by averaging σ_{xy}. Instead of iterating through each element, which incurs significant computational costs, we utilized reaction forces to calculate the average stress components. This approach is feasible as we treat the structure as a unified building block, neglecting internal stress phenomena and operating within the elastic material range. A comparison reveals that both approaches yield average stresses within a 5% margin of difference, but employing the reaction force approach reduces computational time by approximately 98%. Using the reaction force approach, the average stress $\bar{\sigma}_{xx}$ in the compression load case for example can be computed using the following equation:

$$\bar{\sigma}_{xx} = \frac{\sum F_x|_{x=0}}{A} \qquad \text{with} \qquad A = 50\,\mu\text{m} \times 50\,\mu\text{m} \tag{13}$$

Further information on the applied boundary conditions and FEA models can be found in the Supplementary Figure 1 and Figure 2 and elsewhere[46,52,65]. Utilizing the simulations and effective stiffness properties, the cost function values for isotropy and auxeticity can be determined. To identify the optimal set of categorical parameters, the PyAnsys code developed in this study was combined with a multi-objective optimization algorithm in Python. This allows all components of the optimization problem to operate within the same Python environment.

To minimize the objective function, we approach the problem of categorical variables as follows:

Let $\boldsymbol{\omega}_{opt}$ denote the argument that minimizes $f(\boldsymbol{\omega})$ within the combinatorial space, where $f(\boldsymbol{\omega})$ represents the objective functions for isotropy and auxeticity, visualized as green line in Fig. 10b. The categorical variable vector is defined as $\mathbf{z} = [\omega_1,...,\omega_m]$, with m variables in total. The space is a set of possible combinations. Each categorical variable can take a value from $\{U_1,...,U_j\}$, which consists of unordered categories that cannot be ranked on the real-number line. In our case for the $5 \times 5 \times 5$ cubic symmetric lattice $m = 10$ and $j = 8$, for 8 different input unit cell states. The objective is to discover an optimal isotropic and auxetic structure on the line, as depicted in the inset in Fig. 10b.

In the context of practical engineering problems, evaluating the objective function $f(\boldsymbol{\omega})$ can be prohibitively expensive. Furthermore, the challenges of optimization are amplified by the high dimensionality of the design space, making it impractical to optimize certain problems using traditional optimization techniques. Moreover, gradient-based algorithms are not applicable to combinatorial problems. Since the entire process is fully automated and each iteration loop only takes a few minutes, the focus is on reliably finding optimal structures rather than minimizing the number of iteration loops. To address the optimization problem, the NSGA-II was employed[47]. The NSGA-II algorithm is a popular choice for solving multi-objective categorical problems. Its effectiveness in handling categorical variables and ability to optimize conflicting objectives simultaneously make it an ideal choice for such problems. NSGA-II combines genetic operators like selection, crossover, and mutation with a non-dominated sorting procedure to evolve a diverse set of solutions that represent the trade-off between the objectives. By efficiently exploring the combinatorial search space, NSGA-II identifies a set of Pareto-optimal solutions, providing decision-makers with a range of options to choose from based on their preferences and priorities[47]. The population in our current approach consists of two components: the elite individuals and the offspring points, totaling 20 in size. The elite individuals, which are non-dominated points, make up no more than 50% of the population and are inherited from the previous generation. The offspring points are generated through selection, crossover, and mutation processes to create the next generation. The probability of crossover is set to 0.9, while the probability of mutation is set to 0.1. After generating the population, a fitness evaluation was conducted to determine the placement of the design points. The population was iteratively updated until convergence is achieved.

Fabrication

The microlattice structures are fabricated using a hybrid organic-inorganic resin. Details about the mixture, composition and mechnical testing can be found in the Supplementary Methods and Figure 3. The MPL fabrication of the structures for mechanical testing is achieved through sub-micron resolution direct femtosecond laser writing, utilizing a FemtoFiber pro NIR laser with a wavelength of 780 nm, pulse width of 100 fs, and repetition rate of 80 MHz. Details about the MPL setup can be found in the SI. A parametric study is conducted to determine the optimal laser power and writing speed for achieving the best printing results of the microlattices. The laser

output energy during the fabrication process is measured at 6 mW before the objective lens, while the scanning speed is set to 35 $\mu m\ s^{-1}$. The resin sample was secured on a stage equipped with piezo and servo elements, enabling movements in the XYZ directions. A camera is utilized to locate the substrate surface, specifically defined as the bottom of the fabricated structure. By accurately identifying the substrate surface, the camera assists in ensuring the alignment and positioning of the laser writing process. This step is essential for achieving the desired structural integrity and dimensional accuracy of the microlattices. Furthermore, the camera enables in situ monitoring of the polymerization process. It captures real-time videos of the fabrication procedure, allowing researchers to observe the formation of the microlattice structure as it progresses. This monitoring capability is valuable for assessing the quality of the fabrication process and detecting any potential complications or irregularities that may arise during the polymerization. In addition to its primary functions, the camera serves as a tool for early detection of issues such as laser misalignment, material defects, or other factors that could affect the quality of the fabricated microlattices. For a more visual demonstration of the in situ camera imaging during the fabrication of a microlattice, a representative video has been included in the Supplementary Video 10. This video provides a detailed insight into the fabrication process, showcasing the dynamic formation of the microlattice structure and illustrating the real-time monitoring capabilities facilitated by the camera.

Mechanical testing and characterization

In order to assess the mechanical performance of the microlattice structures, in-situ nanoindentation tests were conducted using the PI 87 SEM PicoIndenter from Hysitron. The tests were performed inside a SEM, specifically the FEI Scios 2 model from Thermo Fisher Scientific. A molybdenum flat tip indenter with a diameter of 70 μm, obtained from Probing Solutions Inc., was utilized for all mechanical tests. In order to enhance the imaging quality, the samples were subjected to a gold-platinum sputtering process for a duration of 50 seconds using the Magnetron Sputtering Deposition System. To ensure proper fixation, the microlattice structures were mounted on glass substrates using PELCO® Pro C100 Cyanoacrylate Glue from TED PELLA and fixed onto an SEM pin stub mount. Compression tests were conducted with the top face of the structure in contact with the indenter. Each structure underwent deformation at a rate of 250 $nm\ s^{-1}$, and multiple tests were conducted on each structure to ensure repeatability. To analyze the critical deformation events, a frame-by-frame comparison of the deformation with the force-displacement curve was performed. This testing methodology aligns with previous studies and allows for a comprehensive understanding of the mechanical behavior of the microlattice structures[56].

DATA AVAILABILITY

Supplementary material related to this article can be found online at the corresponding doi. Numerical data supporting the plots and relevant results within this paper are available at: https://github.com/jackyrli/Auxetic-Isotropy-Data.

CODE AVAILABILITY

Complete developed PyAnsys Mechanical APDL and Python optimization code is available from the corresponding author on reasonable request.

Received: 23 August 2023; Accepted: 5 December 2023;
Published online: 03 January 2024

REFERENCES

1. Geng, Q., Wang, D., Chen, P. & Chen, S.-C. Ultrafast multi-focus 3-D nanofabrication based on two-photon polymerization. *Nat. Commun.* **10**, 2179 (2019).
2. Jonušauskas, L. et al. Mesoscale laser 3D printing. *Opt. Express* **27**, 15205–15221 (2019).
3. Balena, A., Bianco, M., Pisanello, F. & De Vittorio, M. Recent advances on high-speed and holographic two-photon direct laser writing. *Adv. Funct. Mater.* **33**, 2211773 (2023).
4. Ouyang, W. et al. Ultrafast 3D nanofabrication via digital holography. *Nat. Commun.* **14**, 1716 (2023).
5. Surjadi, J. U. et al. Mechanical metamaterials and their engineering applications. *Adv. Eng. Mater.* **21**, 1800864 (2019).
6. Gao, H., Ji, B., Jäger, I. L., Arzt, E. & Fratzl, P. Materials become insensitive to flaws at nanoscale: Lessons from nature. *Proc. Natl. Acad. Sci.* **100**, 5597–5600 (2003).
7. Jang, D. & Greer, J. R. Transition from a strong-yet-brittle to a stronger-and-ductile state by size reduction of metallic glasses. *Nat. Mater.* **9**, 215–219 (2010).
8. Meza, L. R., Das, S. & Greer, J. R. Strong, lightweight, and recoverable three-dimensional ceramic nanolattices. *Science* **345**, 1322–1326 (2014).
9. Zhang, X., Vyatskikh, A., Gao, H., Greer, J. R. & Li, X. Lightweight, flaw-tolerant, and ultrastrong nanoarchitected carbon. *Proc. Natl. Acad. Sci.* **116**, 6665–6672 (2019).
10. Bauer, J., Schroer, A., Schwaiger, R. & Kraft, O. Approaching theoretical strength in glassy carbon nanolattices. *Nat. Mater.* **15**, 438–443 (2016).
11. Overvelde, J. T. B., Weaver, J. C., Hoberman, C. & Bertoldi, K. Rational design of reconfigurable prismatic architected materials. *Nature* **541**, 347–352 (2017).
12. dell'Isola, F., Giorgio, I., Pawlikowski, M. & Rizzi, N. L. Large deformations of planar extensible beams and pantographic lattices: heuristic homogenization, experimental and numerical examples of equilibrium. *Proc. Math. Phys. Eng. Sci.* **472**, 20150790 (2016).
13. Turco, E., Misra, A., Pawlikowski, M., dell'Isola, F. & Hild, F. Enhanced Piola–Hencky discrete models for pantographic sheets with pivots without deformation energy: numerics and experiments. *Int. J. Solids Struct* **147**, 94–109 (2018).
14. Song, J. et al. Octet-truss cellular materials for improved mechanical properties and specific energy absorption. *Mater. Des.* **173**, 107773 (2019).
15. Yeung, C. et al. A 3D-printed microfluidic-enabled hollow microneedle architecture for transdermal drug delivery. *Biomicrofluidics.* **13**, 064125 (2019).
16. Li, J. et al. Two-photon polymerisation 3D printed freeform micro-optics for optical coherence tomography fibre probes. *Sci. Rep.* **8**, 14789 (2018).
17. Yin, S. et al. Strong and tough bioinspired additive-manufactured dual-phase mechanical metamaterial composites. *J Mech Phys Solids.* **149**, 104341 (2021).
18. Wegst, U. G. K., Bai, H., Saiz, E., Tomsia, A. P. & Ritchie, R. O. Bioinspired structural materials. *Nat. Mater.* **14**, 23–36 (2015).
19. Fernandes, M. C., Aizenberg, J., Weaver, J. C. & Bertoldi, K. Mechanically robust lattices inspired by deep-sea glass sponges. *Nat. Mater.* **20**, 237–241 (2021).
20. Peng, X. et al. Bioinspired Strategies for Excellent Mechanical Properties of Composites. *J. Bionic. Eng.* **19**, 1203–1228 (2022).
21. Ginzburg, D., Pinto, F., Iervolino, O. & Meo, M. Damage tolerance of bio-inspired helicoidal composites under low velocity impact. *Compos. Struct.* **161**, 187–203 (2017).
22. Zhang, X. et al. Dynamic crushing responses of bio-inspired re-entrant auxetic honeycombs under in-plane impact loading. *Mater. Today Commun.* **23**, 100918 (2020).
23. Frolich, L. M., LaBarbera, M. & Stevens, W. P. Poisson's ratio of a crossed fibre sheath: the skin of aquatic salamanders. *J. Zool.* **232**, 231–252 (1994).
24. Marvi, H. & Hu, D. L. Friction enhancement in concertina locomotion of snakes. *J. R. Soc. Interface* **9**, 3067–3080 (2012).
25. Santulli, C. & Langella, C. Study and development of concepts of auxetic structures in bio-inspired design. *Int. J. Sustain. Des.* **3**, 20 (2016).
26. Wang, Y., Naleway, S. E. & Wang, B. Biological and bioinspired materials: Structure leading to functional and mechanical performance. *Bioact. Mater.* **5**, 745–757 (2020).
27. Pham, M.-S., Liu, C., Todd, I. & Lertthanasarn, J. Damage-tolerant architected materials inspired by crystal microstructure. *Nature* **565**, 305–311 (2019).
28. Maurizi, M., Gao, C. & Berto, F. Inverse design of truss lattice materials with superior buckling resistance. *NPJ Comput. Mater.* **8**, 247 (2022).
29. Kumar, S., Tan, S., Zheng, L. & Kochmann, D. M. Inverse-designed spinodoid metamaterials. *NPJ Comput. Mater.* **6**, 73 (2020).
30. Gross, A., Pantidis, P., Bertoldi, K. & Gerasimidis, S. Correlation between topology and elastic properties of imperfect truss-lattice materials. *J Mech Phys Solids* **124**, 577–598 (2019).
31. Pan, C., Han, Y. & Lu, J. Design and optimization of lattice structures: A review. *Appl. Sci.* **10**, 6374 (2020).
32. Lei, M. et al. 3D Printing of Auxetic Metamaterials with Digitally Reprogrammable Shape. *ACS Appl. Mater. Interfaces* **11**, 22768–22776 (2019).
33. Feng, J., Liu, B., Lin, Z. & Fu, J. Isotropic porous structure design methods based on triply periodic minimal surfaces. *Mater. Des.* **210**, 110050 (2021).
34. Berger, J. B., Wadley, H. N. G. & McMeeking, R. M. Mechanical metamaterials at the theoretical limit of isotropic elastic stiffness. *Nature* **543**, 533–537 (2017).

35. Tancogne-Dejean, T., Diamantopoulou, M., Gorji, M. B., Bonatti, C. & Mohr, D. 3D plate-lattices: an emerging class of low-density metamaterial exhibiting optimal isotropic stiffness. *Adv. Mater.* **30**, 1803334 (2018).
36. Hou, X., Hu, H. & Silberschmidt, V. A novel concept to develop composite structures with isotropic negative poisson's ratio: Effects of random inclusions. *Compos Sci Technol* **72**, 1848–1854 (2012).
37. Chen, W. et al. Stiff isotropic lattices beyond the maxwell criterion. *Sci. Adv.* **5**, 1937 (2019).
38. Chen, D., Skouras, M., Zhu, B. & Matusik, W. Computational discovery of extremal microstructure families. *Sci. Adv.* **4**, 7005 (2018).
39. Agrawal, G., Gupta, A., Chowdhury, R. & Chakrabarti, A. Robust topology optimization of negative poisson's ratio metamaterials under material uncertainty. *Finite Elem. Anal. Des.* **198**, 103649 (2022).
40. Tancogne-Dejean, T. & Mohr, D. Elastically-isotropic truss lattice materials of reduced plastic anisotropy. *Int. J. Solids Struct.* **138**, 24–39 (2018).
41. Panetta, J. et al. Elastic textures for additive fabrication. *ACM Trans. Graph.* **34**, 135–113512 (2015).
42. Chang, Y., Wang, H. & Dong, Q. Machine learning-based inverse design of auxetic metamaterial with zero poisson's ratio. *Mater. Today Commun.* **30**, 103186 (2022).
43. Chen, X. et al. Optimal isotropic, reusable truss lattice material with near-zero poisson's ratio. *Extreme Mech. Lett.* **41**, 101048 (2020).
44. Zheng, X., Chen, T.-T., Guo, X., Samitsu, S. & Watanabe, I. Controllable inverse design of auxetic metamaterials using deep learning. *Mater. Des.* **211**, 110178 (2021).
45. Wilt, J., Yang, C. & Gu, G. Accelerating auxetic metamaterial design with deep learning. *Adv. Eng. Mater* **22**, 1901266 (2019).
46. Sheikh, H. M. et al. Systematic design of cauchy symmetric structures through bayesian optimization. *Int. J. Mech. Sci.* **236**, 107741 (2022).
47. Deb, K., Pratap, A., Agarwal, S. & Meyarivan, T. A fast and elitist multiobjective genetic algorithm: Nsga-ii. *IEEE Trans Evol Comput* **6**, 182–197 (2002).
48. Blank, J. & Deb, K. pymoo: Multi-objective optimization in python. *IEEE Access* **8**, 89497–89509 (2020).
49. Gibson, L. J. Cellular solids. *MRS Bull.* **28**, 270–274 (2003).
50. Voigt, W. Lehrbuch der kristallphysik:(mit ausschluss der kristalloptik) **34** (1910).
51. Zener, C. M. & Siegel, S. Elasticity and anelasticity of metals. *J. Phys. Chem.* **53**, 1468–1468 (1949).
52. Xu, S., Shen, J., Zhou, S., Huang, X. & Xie, Y. M. Design of lattice structures with controlled anisotropy. *Mater. Des.* **93**, 443–447 (2016).
53. Deshpande, V. S., Fleck, N. A. & Ashby, M. F. Effective properties of the octet-truss lattice material. *J. Mech. Phys. Solids* **49**, 1747–1769 (2001).
54. Lu, C. et al. Architectural design and additive manufacturing of mechanical metamaterials: A review. *Engineering* **17**, 44–63 (2022).
55. Austermann, J. et al. Fiber-reinforced composite sandwich structures by co-curing with additive manufactured epoxy lattices. *J Compos Sci.* **3**, 53 (2019).
56. Vangelatos, Z. et al. Strength through defects: A novel bayesian approach for the optimization of architected materials. *Sci. Adv.* **7**, 2218 (2021).
57. Norris, A. N. Poisson's ratio in cubic materials. *Proc. Math. Phys. Eng. Sci* **462**, 3385–3405 (2006).
58. Makatura, L. et al. Procedural metamaterials: A unified procedural graph for metamaterial design. *J. ACM.* **42**, 1–19 (2023).
59. Chen, D., Yan, P., Lv, B., Zhao, Y. & Wu, Y. Parallel reaction monitoring to improve the detection performance of carcinogenic 4-methylimidazole in food by liquid chromatography-high resolution mass spectrometry coupled with dispersive micro solid-phase extraction. *Food Control* **88**, 1–8 (2018).
60. Somers, P. et al. Rapid, continuous projection multi-photon 3d printing enabled by spatiotemporal focusing of femtosecond pulses. *Light Sci. Appl.* **10**, 199 (2021).
61. Bauer, J. et al. Nanolattices: An emerging class of mechanical metamaterials. *Adv. Mat.* **29**, 1701850 (2017).
62. Liew, L. et al. Ceramic mems. *J. Am. Ceram. Soc* **80**, 25 (2000).
63. Ballato, A. Poisson's ratio for tetragonal, hexagonal, and cubic crystals. *IEEE Trans. Ultrason. Ferroelectr. Freq. Control* **43**, 56–62 (1996).
64. Mehl, M. J., Klein, B. M. & Papaconstantopoulos, D. A. First-principles calculation of elastic properties. *Intermetal. Compounds* **1**, 195–210 (1994).
65. Tan, P., Tong, L. & Steven, G. P. Behavior of 3D orthogonal woven cfrp composites. Part II. FEA and analytical modeling approaches. *Compos. Part A Appl. Sci. Manuf.* **31**, 273–281 (2000).

ACKNOWLEDGEMENTS

Support to this work by the US National Science Foundation under grant 2134534 and 2124826 is gratefully acknowledged. B. B acknowledges support from the NSF Graduate Research Fellowship (DGE 2146752). SEM images were obtained using the Scios 2 DualBeam, and HIM images were acquired using the Zeiss ORION NanoFab, which are available at the Biomolecular Nanotechnology Center of the California Institute for Quantitative Biosciences, UC Berkeley. We extend our sincere appreciation to Prof. Hosemann for generously granting us access to the PI-87 Picoindenter and to Frances Allen for her invaluable guidance and expertise in HIM imaging. We also acknowledge Prof. Papadopoulos for providing guidance on FEA simulation and mechanical analysis, as well as Prof. Koumoutsakos and P. Weber for their valuable input on the optimization scheme.

AUTHOR CONTRIBUTIONS

T.M.: Conceptualization, Data curation, Formal analysis, Investigation, Methodology, Software, Validation, Visualization, Writing - original draft, Writing - review & editing. R.L.: Data curation, Formal analysis, Investigation, Methodology, Software, Validation, Visualization, Writing - original draft, Writing - review & editing. (These authors contributed equally to this work.) S.M.: Data curation, Investigation, Methodology, Validation, Visualization, Writing - original draft, Writing - review & editing. B.B.: Investigation, Methodology, Validation, Visualization, Writing - original draft, Writing - review & editing. Z.V.: Conceptualization, Review & editing. E.Y.: Methodology, Software, Validation, Writing - review & editing. C.G.: Funding acquisition, Project administration, Resources, Supervision, Writing - review & editing.

COMPETING INTERESTS

The authors declare no competing interests.

ADDITIONAL INFORMATION

Supplementary information The online version contains supplementary material available at https://doi.org/10.1038/s41524-023-01186-2.

Correspondence and requests for materials should be addressed to Costas P. Grigoropoulos.

Reprints and permission information is available at http://www.nature.com/reprints

Publisher's note Springer Nature remains neutral with regard to jurisdictional claims in published maps and institutional affiliations.